

Enhancing the low temperature hydrogen sensitivity of nanocrystalline SnO₂ as a function of trivalent dopants

C. Drake, A. Amalu, and J. Bernard

Surface Engineering and Nanotechnology Facility (SNF) Laboratory, Advanced Materials Processing and Analysis Center, Department of Mechanical Materials and Aerospace Engineering, University of Central Florida, 4000 Central Florida Boulevard, Eng 1, Room 381, Orlando, Florida 32826

S. Seal^{a)}

Surface Engineering and Nanotechnology Facility (SNF) Laboratory, Advanced Materials Processing and Analysis Center, Department of Mechanical Materials and Aerospace Engineering, University of Central Florida, 4000 Central Florida Boulevard, Eng 1, Room 381, Orlando, Florida 32826 and Nanoscience and Technology Center, 4000 Central Florida Boulevard, Eng 1, Room 381, Orlando, Florida 32826

(Received 27 November 2006; accepted 12 March 2007; published online 18 May 2007)

The effect of different indium doping concentrations on the room temperature hydrogen sensitivity of nano-SnO₂ is investigated. The role of calcination temperature on the surface morphology, phase transformation, and subsequent impact on the gas sensing behavior of nanocrystalline doped SnO₂ is presented. Differences in grain growth with varying doping amount give an explanation for enhanced sensing that is not always so obvious. Variation in the charge carrier density for indium doped nanocrystalline SnO₂ is calculated as a function of indium concentration in the tin oxide lattice structure. The charge carrier density is correlated to the involved surface species of doped nanocrystalline SnO₂ upon hydrogen gas exposure using Fourier transform infrared spectroscopy.

© 2007 American Institute of Physics. [DOI: 10.1063/1.2732498]

I. INTRODUCTION

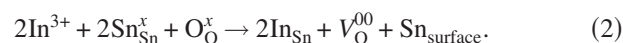
Nanomaterials have been spotlighted for gas sensor applications due to their enhanced abilities over conventional engineering materials. Their high surface to volume ratio greatly enhances the number of sites for gas species to interact with the material. Space charge layer variations in nanostructures make them particularly interesting since adsorption of different gases can control conduction.^{1,2} In spite of these observations, many of the mechanisms responsible for conduction at the nanolevel are still poorly understood.

Doping of the SnO₂ system has been a point of interest due to the ability to tailor electrical and microstructural properties.³⁻⁸ In order to understand the role of doping in nano-oxides, how the particles form, surface chemistry, and material defects will give insight to the material properties, which allow for enhanced gas sensing. Understanding how these material properties affect gas sensing will lead to better engineering of sensor materials and is the focus of this paper.

In order to better understand the role of doping on gas sensor behavior, a technique is needed that will both monitor the surface reaction as well as any changes in electrical properties of the material in question. Fourier transform infrared (FTIR) spectroscopy is such a tool often used to investigate optical properties, mainly absorbance and transmission in the infrared region. Use of the diffuse reflectance mode of the FTIR (DR-FTIR) spectrometer is rare in this type of study. DR-FTIR can be successfully used for studying the surface chemistry variation of materials. However, it can also be used to monitor changes in the free carrier densities of many

semiconductors. Harrick has shown that the use of infrared absorption to measure free carrier densities.⁹ It has been shown that in semiconducting materials, there is an increase in free carriers in the space charge region due to interaction with the reacting gases.¹⁰ This is because upon reaction with the material surface, the gas (depending on whether it is oxidizing or reducing) will either take from or donate electrons to the material. This subsequently leads to variations in DR-FTIR absorbance spectra from semiconductors in the infrared region. Thus, FTIR can be used as an important tool for nano-oxide gas sensing applications.

Previous studies from Shukla *et al.*² have shown an increase in hydrogen detection sensitivity of nanocrystalline SnO₂ when doped with indium (In³⁺). Indium doping creates even more of the desired oxygen vacancies by substitution on a tin lattice site, which in equilibrium expects a 4+ charge to occupy the lattice site. This happens because a 3+ on a 4+ site makes the tin site feel a negative charge. To compensate, an oxygen vacancy will form which causes the previous oxygen site to experience a positive charge. This charge compensation can drastically enhance SnO₂'s gas sensing abilities. Charge modification can be shown using *Kroger-Vink* notations as¹¹



Thus, successful doping of the indium atoms results when it replaces tin into the SnO₂ matrix and this enhances the surface reactivity of the nanoparticles toward gas sensing. In this study, effect of calcination temperature on the particle

^{a)}Electronic mail: sseal@mail.ucf.edu

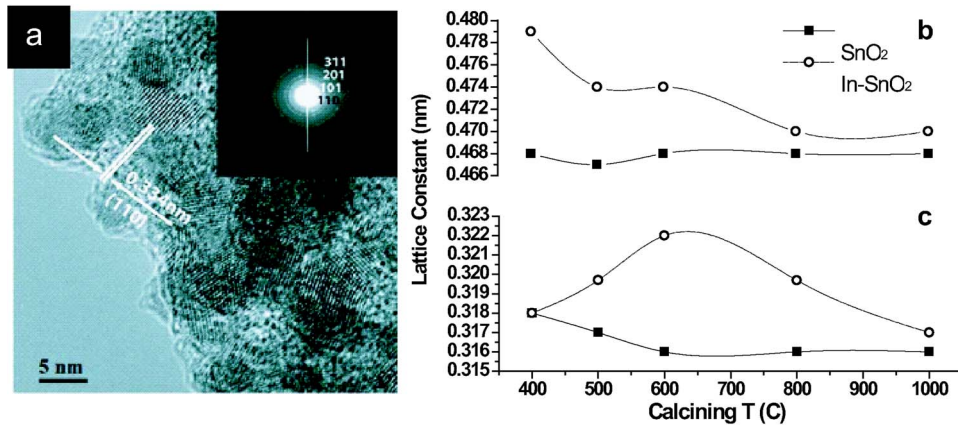


FIG. 1. (a) HRTEM of doped SnO₂ and selected area electron diffraction, (b) lattice constant *a* of SnO₂ and 6.5% In-SnO₂, (c) lattice constant *c* of SnO₂ and 6.5% In-SnO₂.

size evolution, doping of the indium in the SnO₂ matrix, corresponding change in free carrier concentration, and variations in the space charge layer of the nanocrystalline SnO₂ were investigated using *in situ* FTIR Spectroscopy.

II. EXPERIMENT

A. Material preparation

Doped SnO₂ was prepared using sol-gel method.² A sol of tin isopropoxide in isopropanol (72 vol %) and toluene (18 vol %) and indium isopropoxide was prepared. A polymer, hydroxypropyl cellulose (HPC), was added to control grain size during the gelling reaction. The sol is left exposed to air, stirring, until gelling is completed. The gel is then dried at 150 °C for 1 h. Powders were then calcined at 500, 600, 800, and 1000 °C for 1 h in air. The subsequent drying and pyrolysis treatments of the coated polymer nanostructures then result in the decomposition of the polymer structure leaving behind In-SnO₂ nanocrystallites. In the following are the anticipated sol-gel reactions during the drying and pyrolysis procedures²

- (1) $\text{Sn}(\text{OC}_3\text{H}_7)_4 + 4\text{H}_2\text{O} \rightarrow \text{In-Sn}(\text{OH})_4 + 4\text{C}_3\text{H}_7\text{OH}$ (at 25 °C).
- (2) $\text{Sn}(\text{OH})_4 \rightarrow \text{SnO}_2$ (amorphous) + 2H₂O (at 150 °C).
- (3) SnO_2 (amorphous) \rightarrow SnO₂ (crystalline) (at 400 °C).

B. Material characterization

1. X-ray diffraction

Phase transformation and particle size variation of the doped SnO₂ particles were studied using x-ray diffraction (Rigaku model) with a Cu K α ₁ radiation and the optimized operating conditions of 30 mA and 35 kV. The scan rate was set at 2.5 deg/min with a step size of 0.05°.

2. High resolution transmission electron microscopy

The microstructure of the nanoparticles was determined by high resolution transmission electron microscopy (HRTEM) [Philips (Tecnai series)] operated at 300 kV accelerating voltage. Figure 1(a) shows the HRTEM image of In doped SnO₂ particles calcinated at 500 °C. Comparison between the particle size observed by TEM and calculated using x-ray diffraction (XRD), it was observed that each indi-

vidual grain was a single crystal, helping to reduce the barriers for conduction of the free carriers. Due to this very reason, the space charge variations can be considered the dominating conduction mechanism. The selected area electron diffraction (SAED) pattern shown in Fig. 1(a) confirms the growth of the In-SnO₂ particles in the (110) plane of the cassiterite structure.

3. Fourier transform infrared spectroscopy

Doping effects on the space charge layer variation of nanomaterials, as well as how doping effects the surface species present on the material, can both be monitored with the use of FTIR spectroscopy. In this study, indium at various doping amounts (1%, 3%, 6.5%, and 9%) is being investigated. Upon exposure to a reducing gas such as hydrogen, which can donate electrons to the material, the oxygen vacancies are available for transport of the charge, reducing the resistivity. Fourier transform infrared spectrometer (Perkin Elmer) using a Harrick Praying Mantis accessory (used in diffuse reflectance measurements) was used to determine the gas sensing ability of the doped particles as well as calculate the free carrier concentrations. The sample powders (2%) were dispersed in KBr (98%) and tested for hydrogen sensitivity at 30 °C. The spectral resolution was 4 cm⁻¹. All samples were cleaned at 200 °C under vacuum for 15 min and allowed to cool to room temperature before commencing hydrogen gas tests.

III. RESULTS AND DISCUSSION

A. Structure of In doped SnO₂ nanocrystallites

The average crystallite sizes at different calcining temperatures were determined using the SnO₂ (110) diffraction peak and the Scherrer equation:

$$D = \lambda K / \beta \cos \theta, \quad (3)$$

where λ is the wavelength (Cu K α ₁ radiation), θ is the diffraction angle, K is a constant, and β is the full width at half maximum. All of the indium doped SnO₂ samples were nanocrystalline in nature after calcination, Table I. Dominant peaks at (110), (101), and (211) confirm the cassiterite structure of nanocrystalline SnO₂ that is preferred for gas sensing applications. The rutile crystal structure of tin oxide has a tetragonal unit cell with a space group symmetry of

TABLE I. Variation in crystallite size of indium doped SnO₂ ($\pm 5\%$ error).

Calcining <i>T</i> (°C)	Crystallite sizes (nm)			
	1% In	3% In	6.5% In	9% In
500	4	4	3	3
600	5	5	4	4
800	8	8	6	10
1000	13	14	19	23

P42/mnm. The lattice constants are $a=b=4.731$ Å and $c=3.189$ Å. In the tin oxide matrix, Sn atoms are sixfold coordinated to threefold coordinated oxygen atoms. A few extra peaks not associated with the cassiterite structure appear to be beginnings of a not fully formed In₂O₃ (bixbyite) structure at calcination temperatures above 800 °C, Fig. 2. These peaks do not appear for the undoped SnO₂ particles, Fig. 2. This would indicate an amorphous In₂O₃ structure on the surface of the SnO₂ particles that segregates at higher calcining temperatures. At lower calcining temperatures, complete doping of the indium into the structure seems likely. A similar effect has been reported by Carreño *et al.*¹² for rare earth (Ce, Y, and La) doped SnO₂ nanoparticles. The rare earth dopants are segregated to the particle surface at temperatures above 900 °C.

B. Variation in SnO₂ lattice parameter

HRTEM was used to analyze the effective grain size, Figs. 1(b) and 1(c). The lattice constants a and c were analyzed from the selected area electron diffraction to gain understanding of doping on the microstructure evolution. The normal lattice constants are $a=b=4.731$ Å and $c=3.189$ Å. It can be observed that for the undoped SnO₂, the lattice parameter a remains fairly constant. For the 6.5% In doped SnO₂, the lattice constant a decreases with increasing calcination temperature. For undoped SnO₂, the lattice constant c again remains fairly constant. The values of a and c are low compared to published values for SnO₂ and may be due to an oxygen deficient structure. The difference in the trends between a and c may have occurred because the lattice strain that was induced from charge compensation was more pro-

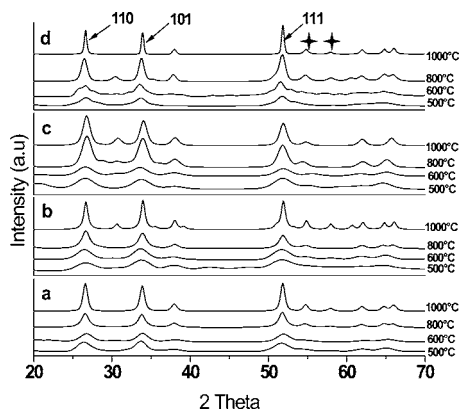


FIG. 2. XRD of SnO₂ samples doped with (a) 1% In, (b) 3% In, (c) 6.5% In, (d) 9% In. \blacktriangle indicates In₂O₃.

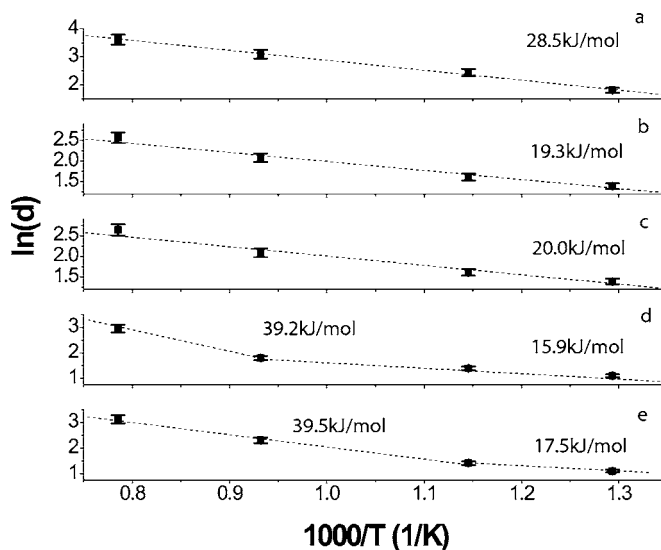


FIG. 3. Plot of $\ln D$ vs $1000/T$ for (a) SnO₂, (b) 1% In doped SnO₂, (c) 3% In doped SnO₂, (d) 6.5% In doped SnO₂, and (e) 9% In doped SnO₂.

nounced in one of these directions in order to minimize the energy of the system. It can be observed that the largest lattice constants belong to the 6.5% In–SnO₂ samples calcined at 600 °C. This seems to indicate that the enlarged cell structure is due to a maximum accommodation of indium atoms into the SnO₂ lattice. The decreasing lattice constants with increasing calcination temperature suggest that a lower amount of indium is doped into the structure at these calcination temperatures.

C. In–SnO₂ grain growth

A plot of $\ln(D)$ (where D is the average crystallite size) versus inverse temperature was used to determine the activation energy for particle growth. For plain sol-gel derived SnO₂, an activation energy of 28 kJ/mol was determined, Fig. 3(a). For samples doped with 1% and 3% indium, the activation energies dropped to 19.3 and 20 kJ/mol, respectively [Figs. 3(b) and 3(c)]. This drop in energy may be associated with an increase in oxygen vacancies created upon indium doping into the SnO₂ lattice. Starting materials (pre-calcination) for nanocrystalline materials tend to be extremely structurally disordered and have been attributed¹³ to oxygen vacancies as well as disordered interfaces. It has been suggested¹⁴ that the low activation energy of nanocrystalline materials may be due to the large percent of highly disordered interfaces. Doping likely increases this disorder, as well as creating more oxygen vacancies for material transport during material synthesis. Though solute drag is usually expected at low doping concentrations (which in turn increases the activation energy for growth), high disorder and oxygen vacancy concentrations likely outweigh this effect at very small grain sizes. This would explain the lower activation energies experienced by samples doped at 1% and 3%.

For SnO₂ samples doped at 6.5% and 9%, two different activation energies appear to be present, Figs. 3(d) and 3(e). For the 6.5% doped samples, an activation energy of 15.9 kJ/mol occurs for the lower calcining temperatures, while at higher temperatures, the activation energy increases

to 39.2 kJ/mol. This appears again with the 9% doped samples, with a lower activation energy of 17.5 kJ/mol at the lower calcination temperatures and a higher activation energy of 39.5 kJ/mol at higher calcination temperatures. This is likely due to the segregation of indium out of the SnO₂ lattice structure (around a calcining temperature of 800 °C) and into the grain boundaries. XRD plots are in agreement (Fig. 3) and give evidence of this phenomenon with increasing doping concentration as well as calcination temperature. The lower initial energies may be attributed to the structural disorder caused by the indium doping into the SnO₂ lattice as previously stated. At higher calcination temperatures, higher diffusion rates coupled with desorption of surface species (H₂O, OH⁻, and CO₂) may lead to segregation of indium to the grain boundaries and particle surface, consequently leading to the formation of amorphous In₂O₃. This would account for the higher activation energies at the higher calcination temperatures due to a grain boundary barrier inhibiting mass transport, and therefore, increasing the energy required for material movement during particle growth.

It has been documented that the mass transport mechanism at temperatures below 1000 °C for the SnO₂ system is due to surface diffusion during particle growth.^{14,15} Because this mass transport mechanism is sensitive to surface contamination, formation of In₂O₃ at the surface of grains would account for this change to higher activation energies at higher calcination temperatures. Leite *et al.*¹⁵ attributed higher growth exponents to surface contamination, or chemical species bonded to the powder surface.

To give more insight to the mass transport mechanism of the In–SnO₂, samples doped at 6.5% were calcined at 30 min, and 1, 3, 5, and 7 h to obtain grain growth kinetics. Generally, grain growth follows

$$G^n = G_o^n + Kt, \quad (4)$$

where G_o is the initial average grain size, G is the average grain size at time t , and K is a constant. The constant K is temperature dependent and is associated with an activation energy component. The grain growth exponent n describes the mechanism for grain growth. Generally, n lies in the range of 2–4, and in many ceramics, n equal to 3 have been observed.¹⁶ In nanocrystalline materials, many different values of n have been reported. Large grain growth exponents and low activation energies are commonly reported for nanocrystalline ceramic materials.

A plot of $\ln(G)$ vs $\ln(t)$ was analyzed to solve for the growth exponent n , Fig. 4. It can be seen that with increasing calcination temperature, the curves shift up, with the 500 °C samples at the bottom and the 1000 °C samples on the top of the figure. The samples calcined at 600, 800, and 1000 °C have similar slopes while the 500 °C samples had a slightly different slope. The calculated values of the growth exponent were $n=2.6$ for the 500 °C samples, $n=4.2$ for the 600 °C samples, $n=4.7$ for the 800 °C samples, and $n=4.4$ for the samples calcined at 1000 °C. Growth exponents in nanocrystalline systems are often reported at 4 or higher, especially in the SnO₂ system.^{14,15} The 600, 800, and 1000 °C samples seem to follow this trend and grow by the same

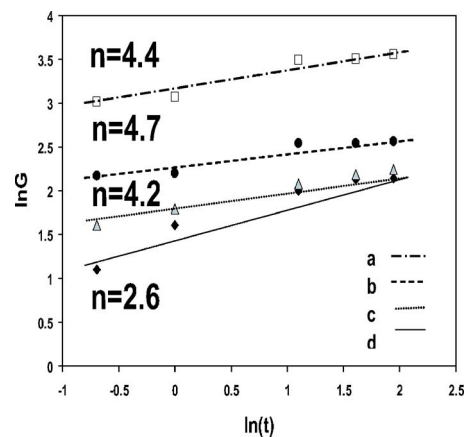


FIG. 4. Plot of $\ln(G)$ vs $\ln(t)$ for 6.5% In–SnO₂ samples calcined at (a) 1000 °C, (b) 800 °C, (c) 600 °C, and (d) 500 °C.

mechanism. For the samples calcined at 500 °C, the value of $n=2.6$ seems to indicate a mixed mechanism. For $n=2$, normal grain growth occurs in a pure, single phase system. For $n=3$, grain growth occurs in the presence of solutes.¹⁴ This could be the case for the samples calcined at 500 °C, solutes hindering growth in a single phase system. For the other three calcination temperatures, the growth mechanism can be attributed to growth in the presence of solutes.¹⁷ This would explain, from peak evolution in XRD, the changes in activation energy with increasing calcination temperature. As calcination temperature was increased at the higher doping amounts of 6.5% and 9%, the activation energy for growth was increased, indicating impediment to atomic movement. This would align with indium segregating to the surface/grain boundaries by a surface diffusing mechanism. Combined, the different activation energies and growth exponents lead to explanations of the different gas sensing behaviors between the different dopings and different calcination temperatures. The variation in gas sensing will be impacted by the surface structure of the SnO₂ grains based on synthesis of the material. By changing the amount of doping in the SnO₂ system, changes in the way the grains form and subsequently grow will affect the type of final surface structure achieved. This allows for engineering of the surface more precisely to specific applications.

D. Hydrogen sensing behavior of In–SnO₂

The surface reactions in gas sensor applications play a vital role in tuning a material to a target gas. FTIR is a useful tool to monitor both the surface reactions upon introduction of a target gas, as well as monitor changes in the electrical properties of the material being tested. FTIR absorbance data were used in this study to calculate both the electrical conductivity and the major free carrier concentrations for In–SnO₂ samples. Beer's Law, which shows that absorbance is directly related to the absorption coefficient, is used to calculate the absorption coefficient, Eq. (5).

$$I = I_o \exp(-Kx). \quad (5)$$

In the above equation, x is the thickness of the measured sample and K represents the absorption coefficient. Drude-

Zener theory was used to calculate the conductivity as well as the major free carrier concentration using the relationship

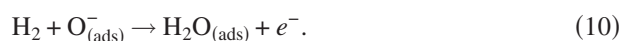
$$K = \frac{1}{\epsilon_o c_o n} \frac{\sigma^2 q^2}{\omega^2 m^2 \mu^2} = \lambda_o^2 \frac{\sqrt{\mu_o}}{\sqrt{\epsilon_o}} \frac{Nq^3}{4\pi^2 nm^2 c_o^2 \mu}. \quad (6)$$

The K here is the absorption coefficient taken from Beer-Lambert's law. For Eq. (6), N is the free carrier concentration (m^{-3}), σ is the electrical conductivity (S/m), ω is the angular frequency, m is the carrier effective mass (kg), μ is the carrier mobility [$m^2/(V s)$], n is the index of refraction, and λ_o is the wavelength in free space ($1/n = \lambda/\lambda_o$). Equation (6) is valid when $\omega t \gg 1$, and $\sigma_o \ll \omega \epsilon'$, which holds true in the infrared region for most semiconducting materials. Drude-Zener theory assumes classical statistics, but quantum effects are important below a critical wavelength at a given temperature. Spitzer *et al.*¹⁸ have shown that the right hand side of Eq. (6) for the absorption coefficient needed to be corrected by multiplication with

$$\sqrt{\frac{h\omega}{2\pi kT}} \quad \text{when} \quad h\omega \gg 2\pi kT. \quad (7)$$

Multiplication by this factor is used in order for quantum effects to be accounted for. This is an important consequence for nanomaterials as they approach smaller and smaller sizes. For low temperatures in the infrared region, this relationship is required. This leads to a $\lambda^{3/2}$ variation with wavelength for the conductivity of oxides in the infrared region.

All indium doped SnO_2 samples were tested for sensitivity to H_2 gas at room temperature (30°C) using the Praying Mantis accessory and the diffuse reflectance mode of the FTIR. It can be observed that there is an upward shift in the absorbance spectra after exposure to H_2 if the material is able to detect the gas. When exposed to air, oxygen molecules are physisorbed onto the surface of nanocrystalline SnO_{2-x} and take free electrons from SnO_{2-x} . A change then occurs to $\text{O}_{2\text{ ads}}^-$ or $\text{O}_{\text{ ads}}^-$ species on the surface. When a reducing gas (such as hydrogen) comes into contact with these nanoparticles, it is oxidized via reaction with the $\text{O}_{2\text{ ads}}^-$ or $\text{O}_{\text{ ads}}^-$ surface species. Subsequently, electrons are reintroduced into the electron depletion layer. The following equations show the surface reactions upon introduction of hydrogen to the SnO_{2-x} surface¹:



Electrons added to the space charge region of an n -type semiconductor surface will lead to an increase in absorption,¹⁹ affecting the broad background of its FTIR spectra. These excess electrons from hydrogen are able to absorb more energy (from the infrared) for conduction, increasing the amount of absorption. The changes in oxygen vacancy concentration with doping concentration are shown in Fig. 5.

All of the In– SnO_2 samples at different dopings were tested for hydrogen sensitivity. Only three of the samples

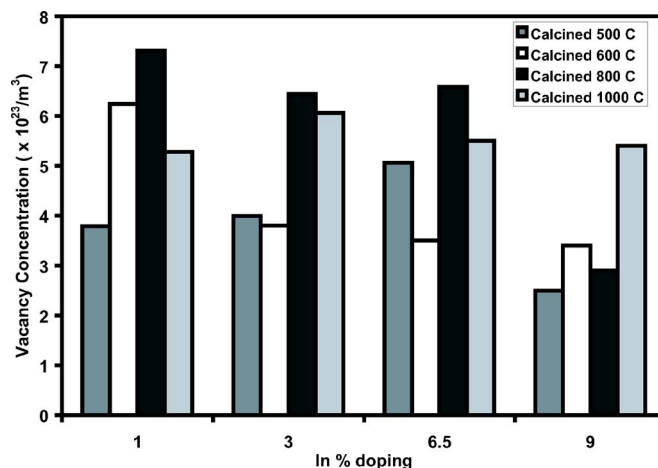


FIG. 5. Variation in oxygen vacancy concentration as a function of percentage doping and calcining temperature. Reported for nano-In– SnO_2 samples tested at 30°C .

showed any appreciable response to H_2 gas exposure at room temperature without the help of a catalyst. These were the 6.5% In– SnO_2 samples calcined at 500 and 600 $^\circ\text{C}$, as well as the 3% In– SnO_2 sample calcined at 500 $^\circ\text{C}$. The greatest response to hydrogen was from the 3% and 6.5% In– SnO_2 samples calcined at 500 $^\circ\text{C}$, but by what appears to be slightly different surface mechanisms, Figs. 6(a) and 6(b). For both samples, an increase in free carriers, and therefore conductivity, can be seen by the increase in absorbance for the broad background. These are areas where surface vibrations are not affected even after introduction of a detectable gas. Only shifts up and down will be seen for the broad background. For the 3% In– SnO_2 , the broad peak around 3450 cm^{-1} (due to physisorbed water bending or surface hydration)³ is altered after H_2 exposure, where on the 6.5% sample surface, water groups are little impacted. Surface CO_2 ($\sim 2300\text{ cm}^{-1}$) (Ref. 20) on the 3% In– SnO_2 samples also appear affected after hydrogen exposure while the same surface group on the 6.5% sample goes unaltered. So even though both samples responded to the hydrogen gas with an

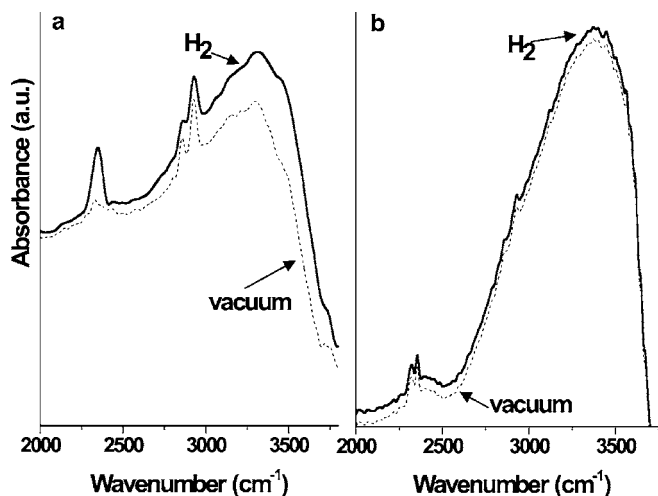


FIG. 6. FTIR absorbance spectra in vacuum and after exposure to hydrogen gas at room temperature for (a) 3% In doped SnO_2 calcined at 500°C and (b) 6.5% In doped SnO_2 calcined at 500°C .

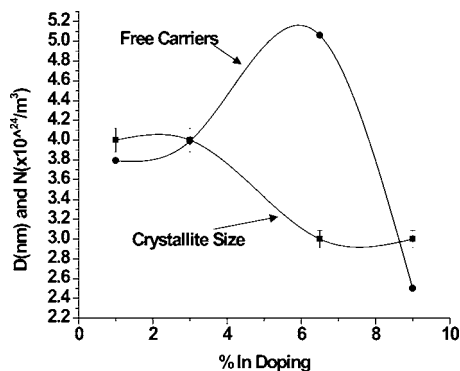


FIG. 7. Change in free carrier density at room temperature and crystallite size with doping amount. Samples calcined at 500 °C.

increase in absorption, it appears that the 3% In-SnO₂ sample uses surface CO₂ and water groups to dissociate, or participate in the dissociation of, adsorbed hydrogen gas. Note that both samples possess the surface groups, but the 3% sample appears to have a slightly greater percentage of surface coverage by these species after exposure to hydrogen. The approximate area under the curve for these peaks is higher for the 3% sample than for the 6.5% sample. The sensing mechanism for the 6.5% In-SnO₂ samples may be due to surface species which are difficult to distinguish using DR-FTIR.

It may be deduced that due to the lower surface coverage of CO₂ and adsorbed water, surface oxygens and vacant oxygen positions may be the mechanisms behind the sensing ability of the 6.5% sample calcined at 500 °C. Both the 3% and 6.5% samples appear to have been fully doped with indium. It is likely that the substituted tin atoms made their way to the surface of the particles, but without full bonding to the oxygen species. This would have left behind surface oxygen vacancies. The vibrations associated with these surface species occur at very low wave numbers of the FTIR and are associated with an appreciable amount of noise, making it difficult to correctly analyze changes in absorbance. This surface information is useful in the engineering of sensor materials to specific applications and environments which may desorb certain surface species required for sensing of a particular gas.

It has been previously reported that the maximum doping of indium into the SnO₂ system is around 3%.²¹ In this study, a change in growth activation energy is also observed when comparing 3% and 6.5% indium doped SnO₂ samples. A comparison of the free carrier density in the space charge region versus indium doping at a calcination temperature of 500 °C is shown in Fig. 7. The 6.5% doped sample calcined at 500 °C has the highest free carrier density with the smallest crystallite/grain size. Though this free carrier density is for the space charge region of the material, due to its very small size, it can be assumed that this space charge region occupies most of the grain. Even though, thermodynamically, 3% is the solid solution limit of indium into the SnO₂ system, it is possible that at higher doping amounts, certain overdopings can be achieved at relatively short calcination times. This may be due to the high degree of disorder already present in the nanomaterial prior to high temperature calci-

nation. This initial disorder in starting materials for nanocrystalline SnO₂ when synthesizing using a bottom-up approach may allow for higher doping amounts than a more atomically ordered crystal lattice would. At short calcination times, since the growth mechanism is reportedly dominated by surface diffusion, the structural disorder within the grains remains, allowing for overdopings from the thermodynamically predicted amounts in this nanosystem.

These overdoping amounts may have the greatest impact on the space charge region for gas sensing applications where the grains are comparable to the Debye length of the material. This is due to the creation of and ability to retain defects above what would be expected for thermodynamically predicted maximum doping amounts for a system in equilibrium. Creation of a larger amount of oxygen vacancies, the charge carriers in the case of nanocrystalline SnO₂, will impact two things. One, the number of surface oxygen vacancies may increase, creating more opportunities for the target gas (in this case hydrogen) to interact with the material. Second, it creates more charge carriers within the material. This gives injected electrons from the surface reaction with hydrogen more opportunities to move about the material. In the case of hydrogen sensing at room temperature, maximizing the number of free carriers in the space charge region leads to better sensing of hydrogen gas upon dissociation on the surface.

IV. CONCLUSION

Two optimal indium doping amounts and calcination temperature for room temperature sensing of hydrogen were brought to light for the nanocrystalline SnO₂ system. Both 3% and 6.5% samples calcined at 500 °C were able to detect hydrogen at room temperature without a catalyst. The samples with 6.5% doping have higher free carrier densities in the space charge region and appear not to rely heavily on surface adsorbed species, such as water and CO₂, for room temperature sensing of hydrogen gas. On the other hand, the 3% doped sample with a lower free carrier density relied greatly on these surface species during dissociation of hydrogen gas on its surface. Thus the mechanism of room temperature hydrogen sensing varies greatly as a function of dopant concentration and alteration in free carrier density in nanocrystalline SnO₂.

ACKNOWLEDGMENTS

Authors gratefully thank NASA NAG 32751, NSF CMS: 0548815, BES: 0541516, NSF REU EEC: 0453436, NASA ASRC, NSF GK-12 fellowship for funding the research.

¹S. Shukla, S. Seal, L. Ludwig, and C. Parish, *Sens. Actuators B* **97**, 256 (2004).

²S. Shukla, S. Patil, S. C. Kuiry, Z. Rahman, T. Du, L. Ludwig, C. Parish, and S. Seal, *Sens. Actuators B* **96**, 343 (2003).

³O. Wurzinger and G. Reinhardt, *Sens. Actuators B* **103**, 104 (2004).

⁴H. Yang, X. Song, X. Zhang, W. Ao, and G. Qiu, *Mater. Lett.* **4299**, 1 (2003).

⁵A. Maciel, P. Lisboa-Filho, E. Leite, C. Paiva-Santos, W. Schreiner, Y. Maniette, and E. Longo, *J. Eur. Ceram. Soc.* **23**, 707 (2003).

⁶H. Yang, S. Han, L. Wang, I. Kim, and Y. Son, *Mater. Chem. Phys.* **56**, 153 (1998).

- ⁷H. Ahn, H. Choi, K. Park, S. Kim, and Y. Sung, *J. Phys. Chem. B* **108**, 9815 (2004).
- ⁸G. Xu, Y. Zhang, X. Sun, C. Xu, and C. Yan, *J. Phys. Chem. B* **109**, 3269 (2005).
- ⁹N. Harrick, *Phys. Rev.* **103**, 1173 (1956).
- ¹⁰N. Harrick, *Phys. Rev.* **125**, 1165 (1962).
- ¹¹A. R. West, *Basic Solid State Chemistry* (Wiley, West Sussex, England, 1999).
- ¹²N. L. V. Carreño, H. V. Fajardo, A. P. Maciel, A. Valentini, F. M. Pontes, L. F. D. Probst, E. R. Leite, and E. Longo, *J. Mol. Catal. A: Chem.* **207**, 89 (2004).
- ¹³K. N. Yu, Y. Xiong, Y. Ciu, and C. Xiong, *Phys. Rev. B* **55**, 2666 (1997).
- ¹⁴C. H. Shek, J. K. L. Lai, and G. M. Lin, *Nanostruct. Mater.* **11**, 887 (1999).
- ¹⁵E. R. Leite, J. A. Cerii, E. Longo, J. A. Varela, and C. A. Paskocima, *J. Eur. Ceram. Soc.* **21**, 669 (2001).
- ¹⁶M. N. Rahaman, *Ceramic Processing and Sintering* (Dekker, New York, 1995).
- ¹⁷J. K. L. Lai, C. H. Shek, and G. M. Lin, *Scr. Mater.* **49**, 441 (2003).
- ¹⁸W. Spitzer, R. Collin, and H. Fan, *Phys. Rev.* **98**, 1536 (1955).
- ¹⁹G. Martinelli and M. Carotta, *Sens. Actuators B* **23**, 157 (1995).
- ²⁰D. Amalric-Popescu and F. Bozon-Verduraz, *Catal. Lett.* **64**, 125 (2000).
- ²¹F. Sensato, R. Custodio, M. Calatayud, A. Beltran, J. Andres, J. Sambrano, and E. Longo, *Surf. Sci.* **511**, 408 (2002).